Regioselective Generation and Reactivity Control of Subnanometric Pt clusters in Zeolites for High-Temperature Catalysis

Lichen Liu,[1] Miguel Lopez-Haro,[2] Christian W. Lopes,[1] Chengeng Li,[1] Patricia Concepcion,[1] Laura Simonelli,[3] Jose J. Calvino[2] and Avelino Corma[1]*

[1] *Instituto de Tecnología Química, Universitat Politècnica de València-Consejo Superior de Investigaciones Científicas, Av. de los Naranjos s/n, Valencia 46022, Spain*

[2] *Departamento de Ciencia de los Materiales e Ingeniería Metalúrgica y Química Inorgánica, Facultad de Ciencias, Universidad de Cádiz, Cádiz, Spain*

[3] *ALBA Synchrotron Light Source, 08290 Cerdanyola del Vallès, Barcelona, Spain*

*Corresponding author. Email: acorma@itq.upv.es

Abstract

Subnanometric metal species (single atoms and clusters) have been demonstrated to be unique compared to their nanoparticulate counterparts. However, the poor stabilization of subnanometric metal species towards sintering at high temperature (>500 ºC) under oxidative or reductive reaction conditions limits their catalytic application. Zeolites can serve as an ideal support to stabilize subnanometric metal catalysts, but it is challenging to localize subnanometric metal species on specific sites and modulate their reactivity. We have achieved a very high preference for localization of highly stable subnanometric Pt and Pt-Sn clusters in the sinusoidal channels of purely siliceous MFI zeolite, as revealed by atomically resolved electron microscopy combining high-angle annular dark-field and integrated differential phase contrast imaging techniques. These catalysts show very high stability, selectivity, and activity for the industrially important dehydrogenation of propane to form propylene. This stabilization strategy could be extended to other crystalline porous materials.

1. Introduction

One frontier in the synthesis of zeolites and in general other microporous materials consists on locating active sites in the desired framework or extra-framework position.[1-4] For instance, in the case of zeolites containing pores and/or cavities of different dimensions, it is clear that locating the active sites selectively in one specific type of pore or cavity is a fundamental challenge with significant implications for their catalytic application, due to differences in geometric and confinement effects. For instance, attempts have been reported to preferentially locate framework Al atoms in the intersectional sites or within the 10MR channels of ZSM-5 (MFI-type zeolite).[5-7] However, when functional metals, such as Pt or Pd, have been introduced by including the metal precursor during the synthesis or through inter-zeolite transformations, nanoparticles of 1-2 nm instead of subnanometric metal species (single atoms or clusters) have been obtained within MFI zeolite.[8-11] As far as we know, the metal particles show random distribution within the zeolite crystallites. From the materials and catalysis point of view, the following challenges remain unsolved: a) to generate stable subnanometric metal species within the zeolite crystallites; b) to stabilize them regioselectively within the 10MR channels; c) to achieve the above goals with purely siliceous MFI zeolite and to avoid the presence of acid sites in the final material. Notice that if these three objectives are achieved, a very regular distribution of metal clusters of ~0.5 nm would be obtained, i.e. with the diameter of the 10MR channels, that would be highly stable against Ostwald ripening sintering, even at high temperature (>550 ºC) under a reductive atmosphere.[12,13] Such type of materials should open new possibilities for a number of catalytic applications, including the very relevant activation of alkanes.[14-17]

It has been demonstrated that subnanometric Pt clusters show higher reactivity than Pt nanoparticles for propane dehydrogenation reaction.[18] However, when Pt clusters are supported on solid carriers with open structures, those Pt clusters may suffer fast deactivation and the subsequent regeneration-reaction cycles will lead to severe sintering of Pt. Therefore, if regular Pt clusters can be regioselectively generated within the 10MR channels of a purely siliceous MFI zeolite, the resultant catalyst should present not only high activity, but a better stability when working under high-temperature conditions.

To achieve this goal, we have carried out one-pot synthesis of Pt-MFI materials. The starting hypothesis was that the template molecules (TPA^+OH^-) will occupy the intersectional voids, hence limiting the access of Pt species to that position. Considering the larger space in the sinusoidal channels

versus the straight channels, Pt species may preferentially be located in the sinusoidal channels. A controllable amount of K^+ is introduced to compensate the silanol groups, and to stabilize the subnanometric Pt species.[19-21] Finally, atomically dispersed Sn species can also be introduced to electronically modify the Pt clusters to increase propylene selectivity for the propane dehydrogenation reaction.

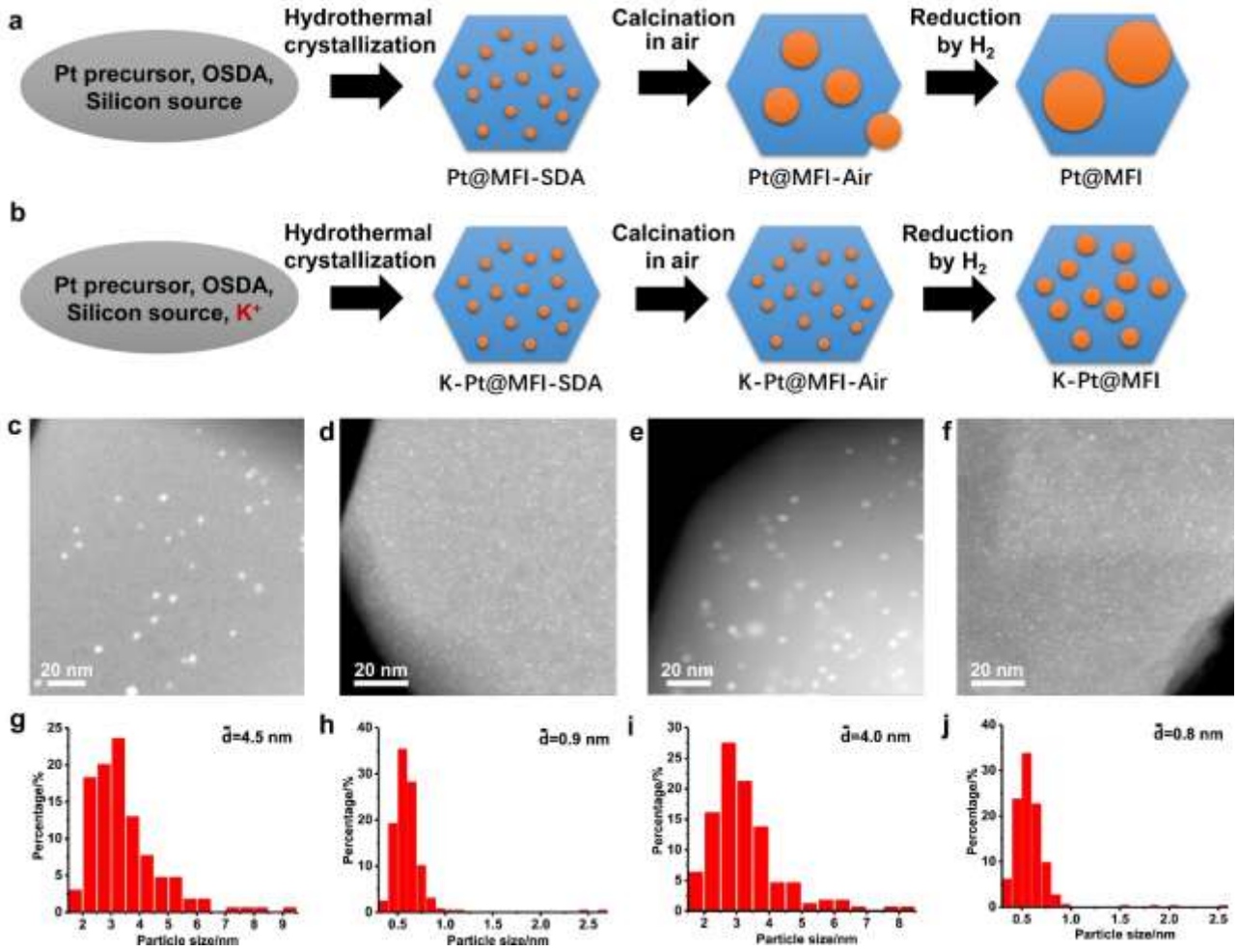

Fig. 1. One-pot synthesis of Pt-zeolite materials. (a, b) Schematic illustration of formation process of Pt@MFI and K-Pt@MFI samples by one-pot synthesis. STEM image of Pt-zeolite samples after reduction by H_2 at 600 °C: K-free Pt-MFI (c), K-Pt@MFI (d), K-free PtSn@MFI (e) and K-PtSn@MFI (f). The size distribution of Pt particles in different Pt-zeolite materials are presented: K-free Pt-MFI (g), K-Pt@MFI (h), K-free PtSn@MFI (i) and K-PtSn@MFI (j). The average particle size is calculated according to $d= \Sigma n_i d_i^3/\Sigma n_i d_i^2$.

2. Results and Discussions

Encapsulation of Pt particles in MFI zeolite.

As illustrated in **Fig. 1a** and **Fig. 1b**, by a one-pot synthesis strategy, Pt species can be encapsulated into purely siliceous MFI zeolite with Pt loading of ~0.4 wt% (**Table S1**). All the Pt-zeolite materials with different chemical compositions show typical diffraction patterns of MFI zeolite (see **Fig. S1**). Interestingly, the presence of K within the synthesis mixture has significantly influenced the size of the encapsulated Pt species. As shown in **Fig. 1c** and **Fig. 1d**, Pt mainly exists as nanoparticles of 3-5 nm in the K-free Pt@MFI sample (**Fig. S2**), while subnanometric Pt clusters of 0.4~0.7 nm are the dominant species in the K-Pt@MFI sample (**Fig. S3**). In order to investigate the role of K, we have firstly characterized the as-synthesized, non-calcined, Pt-zeolite samples (K-Pt@MFI-SDA and Pt@MFI-SDA) obtained in the presence and absence of K, by electron microscopy. As shown in **Fig. S4** and **Fig. S5**, only atomically dispersed Pt species are detected in both samples, as confirmed by image simulation (see **Fig. S6**). Herein, to identify the location of Pt atoms in Pt@MFI-SDA and K-Pt@MFI-SDA, we have employed a combination of high-resolution high-angle annular dark-field scanning transmission electron microscopy (HR HAADF-STEM) and integrated differential phase contrast (iDPC) imaging techniques to simultaneously visualize both Pt atoms and the zeolite structure with atomic resolution.[22,23] As shown in **Fig. S4**, by correlating the HR HAADF-STEM and iDPC images, it can be deduced that most Pt atoms are located in the sinusoidal channels of MFI zeolite structure, whereas a much smaller amount is found in the straight pore channels or at the intersectional voids. This regioselective distribution of Pt species can be caused by the occupation of the intersectional voids by the template (TPA^+), as well as by the availability of larger space in the sinusoidal channels compared to the straight channels (see **Fig. S7**).[24-26] The characteristics of the location of Pt atoms described above are the same when the synthesis is carried out in the presence of K^+ (K-Pt@MFI-SDA sample), indicating that K^+ does not play a relevant role in the encapsulation of atomically dispersed Pt species during the hydrothermal synthesis. This conclusion is also confirmed from the characterization by X-ray absorption spectroscopy (see **Fig. S8** and **Table S2**). A short-distance contribution at ~2.0 Å can be ascribed to Pt-O/N bonding, while the contribution of Pt-Pt bonding is not observed in both samples.

A subsequent calcination in air at 600 °C to remove the organic template in the as-synthesized Pt-

MFI materials gives rise to the formation of Pt nanoparticles in the K-free Pt@MFI-Air sample, indicating the migration and subsequent sintering of Pt (see **Fig. S9**). However, as presented in **Fig. S10**, Pt remains atomically dispersed after calcination in air in the K-Pt@MFI-Air sample. Interestingly, their location within the 10MR sinusoidal channels remains almost unchanged, when compared to the as-synthesized K-Pt@MFI-SDA sample. A main contribution at ~2.0 Å, corresponding to Pt-O bonding, is observed in the extended X-ray adsorption fine structure (EXAFS) spectrum of K-Pt@MFI-Air sample (see **Fig. S11** and **Table S3**) while a typical Pt-Pt bonding at ~2.7 Å is observed in the K-free Pt@MFI-Air sample. The results from STEM-iDPC imaging and X-ray absorption spectroscopy indicate that the role of K is related to the stabilization of Pt atoms during the calcination process, avoiding their sintering into Pt nanoparticles.[19,20]

As shown in **Fig. S12**, the amount of –OH groups in the K-free Pt-zeolite samples measured by IR spectroscopy decreased significantly after the introduction of K.[27] A plausible explanation is that, the –OH groups in the K-free zeolite is replaced to $-O^{-}K^{+}$ species. Furthermore, the presence of $-O^{-}K^{+}$ species can interact with the positive-charged Pt species by forming stabilized -O-Pt species during the high-temperature calcination in air. If the K^{+} in the K-Pt@MFI-Air sample was exchanged by NH_4^{+}, Pt atoms would sinter into Pt nanoparticles in the subsequent calcination at 600 ºC in air and reduction treatment by H_2 at 600 ºC (see **Fig. S13** and **Fig. S14**).

Most interestingly, when the K-containing K-Pt@MFI-Air sample was reduced in H_2 at 600 ºC, Pt atoms turned into subnanometric clusters, as shown in **Fig. 1d**. The low white line intensity in Pt L_3-edge X-ray absorption near-edge structure (XANES) spectrum of K-Pt@MFI sample (**Fig. 2a**) indicates the presence of metallic Pt after the H_2 reduction treatment. The coordination number of first-shell Pt-Pt (N_{Pt-Pt}) bonding for K-Pt@MFI sample is ~6.6 (see **Table 1**), corresponding to an average size of ~0.9 nm (**Fig. 1h**).[28] Considering that the average size of Pt clusters and Pt nanoparticles is ~0.55 nm and ~2 nm respectively, then ~80% of Pt atoms should be located in the internal space of MFI crystallites as subnanometric clusters while ~20% of Pt atoms exist as Pt nanoparticles (according to the following simple estimation: 80%×0.55+20%×2 ≈0.85 nm). In the case of K-free Pt@MFI sample, the first-shell N_{Pt-Pt} is ~10.6, corresponding to an average size of 4-5 nm as shown in **Fig. 1g**.

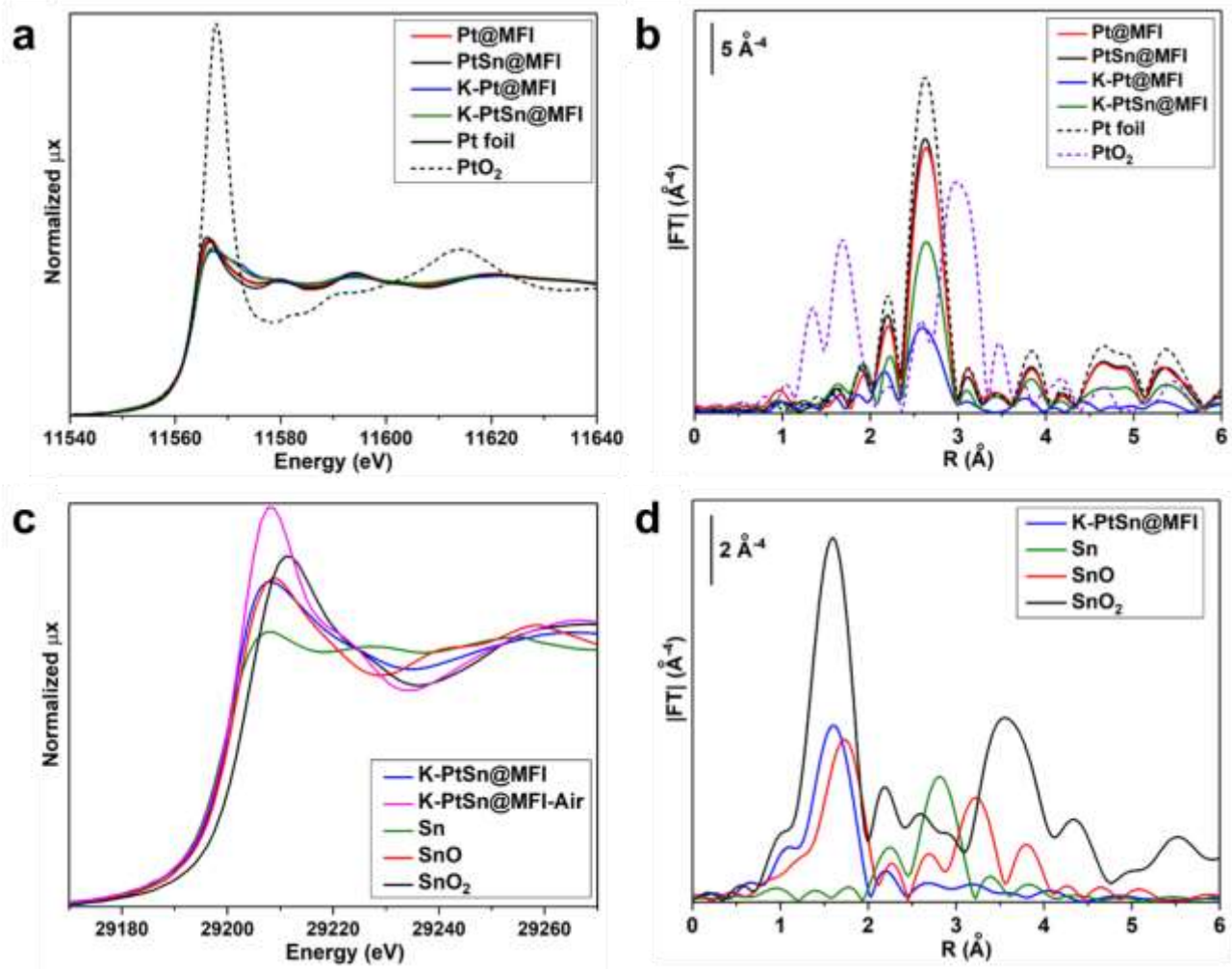

Fig. 2. Characterization of Pt-zeolite materials by X-ray absorption spectroscopy. All the samples are *in situ* reduced by H_2 at 600 ºC before the spectra collection, except for the K-PtSn@MFI-Air sample in (c), which was measured directly without pre-reduction by H_2. The Pt and Sn standard samples were also measured directly. XANES spectra (a) and EXAFS spectra (b) of Pt L_3-edge of different Pt-zeolite samples. (c) Sn K-edge XANES spectra of K-PtSn@MFI-Air and K-PtSn@MFI sample. (d) Sn K-edge EXAFS spectrum of K-PtSn@MFI sample.

Table 1. Fit results of Pt-edge and Sn-edge of EXAFS spectra of various Pt-zeolite materials.

Sample	N_{Pt-Pt}	R_{Pt-Pt} (Å)	σ^2 (Å^2)	ΔE_0 (eV)	R_{factor}
Pt foil	12	2.763 ± 0.001	0.0048 ± 0.0001	6.7 ± 0.5	0.0017
Pt@MFI	10.6 ± 0.6	2.762 ± 0.001	0.0051 ± 0.0002	7.0 ± 0.3	0.0025
PtSn@MFI	10.7 ± 0.4	2.763 ± 0.001	0.0050 ± 0.0001		0.0014
K-Pt@MFI	6.6 ± 1.2	2.743 ± 0.006	0.0074 ± 0.0010		0.0049
K-PtSn@MFI	6.4 ± 0.4	2.768 ± 0.001	0.0049 ± 0.0002		0.0150

Sample	N_{Sn-O}	R_{Sn-O} (Å)	σ^2 (Å^2)	ΔE_0 (eV)	R_{factor}
SnO_2	6	2.055 ± 0.010	0.0023 ± 0.0012	7.3 ± 1.4	0.0044
SnO	4	2.202 ± 0.001	0.0071 ± 0.0012	8.3 ± 0.7	0.0017
K-PtSn@MFI	3.2 ± 0.2	2.061 ± 0.006	0.0058 ± 0.0012	8.1 ± 1.0	0.0037

R, bonding distance; σ^2, Debye−Waller factor; S_0^2, many-body amplitude reduction factor; ΔE_0, inner potential correction; Δk and ΔR are the interval in the k and R space for the Fourier transformation and the fit, respectively.

The fits of Pt edge were performed on the first coordination shell (ΔR=2.0-3.0 Å) over FT of the $k^1k^2k^3$-weighted $\chi(k)$ functions performed in the Δk=3.6-16.7 Å^{-1} interval, resulting into several independent parameters of $2\Delta R\Delta k/\pi$ = 23.8 (7.9 for Pt foil). The standard Pt foil was fitted individually while the samples were fitted using a co-refinement approach resulting into one N_{Pt-Pt}, R and σ^2 for each sample and one common ΔE_0 for all samples. S_0^2 = 0.89. The fit of the Pt-edge EXAFS spectra of Pt-zeolite samples are presented in **Fig. S15** and **Fig. S16**.

The fits of Sn edge were performed on the first coordination shell (ΔR=1.0-2.0 Å) over FT of the $k^1k^2k^3$-weighted $\chi(k)$ functions performed in the Δk=2.8-11.0 Å^{-1} interval, resulting into a number of independent parameters of $2\Delta R\Delta k/\pi$=20.3 for the K-PtSn@MFI sample (5 for both SnO_2 and SnO). SnO_2 S_0^2 = 0.89; SnO S_0^2 = 1.0. The fit of the Sn-edge EXAFS spectrum of K-PtSn@MFI sample are presented in **Fig. S34**.

Determination of the location of subnanometric Pt clusters

Considering the structure of MFI zeolite, one can expect that subnanometric encapsulated Pt clusters may distribute in different locations (including the straight channels, intersectional voids and the sinusoidal channels). Therefore, we have analyzed the HR HAADF-STEM results in further detail. For K-Pt@MFI sample, as displayed in **Fig. 3a** and **3c**, 0.4-0.6 nm Pt clusters can be clearly observed as high-intensity areas along the [010] direction, while the 10MR straight channels appear as low-intensity pores. Corresponding HR HAADF-STEM images in greyscale are shown in **Fig. S17**. However, due to the weak contrast of the zeolite framework and its sensitivity to electron beam, the detailed structure of MFI zeolite is not well revealed in the HR HAADF-STEM image. By using the newly developed iDPC technique, the atomic structure of MFI zeolite can be recorded simultaneously with the HR HAADF-STEM image under low-dose conditions (see **Fig. 3b**).[22,23] As presented in **Fig. 3d**, the detailed structure of MFI zeolite can be clearly identified in the iDPC image, even the 5R units in the framework. Since HR HAADF-STEM imaging is more sensitive to heavy elements (Pt in this work), and the structural information of the zeolite framework is finely captured by iDPC imaging, the precise location of subnanometric Pt clusters can be reliably identified by correlating the paired images. The results demonstrate that Pt clusters of 0.4-0.6 nm are preferentially located in the sinusoidal channels (see more images in **Fig. S18** to **Fig. S22**). The location of Pt clusters has also been confirmed by STEM-iDPC imaging on a zeolite crystallite with the tilted [010] orientation (see **Fig. 3e** to **Fig. 3h**), showing that the subnanometric Pt clusters overlap with the sinusoidal channels.

Synthesis of bimetallic PtSn@MFI

Following the same synthesis procedure, a second metal component such as Sn can be introduced together with Pt. Similar to the situation observed before, after calcination in air, Pt species in the K-free PtSn@MFI sample agglomerate into nanoparticles (see **Fig. S23**) while the Pt species in K-PtSn@MFI sample remain atomically dispersed (see **Fig. S24**), as in the as-synthesized K-PtSn@MFI-SDA sample (see **Fig. S25**). After reduction by H_2 at 600 °C, large Pt nanoparticles are formed in the PtSn@MFI sample (see **Fig. 1e**, **Fig. 1i** and **Fig. S26**) while subnanometric Pt clusters (~0.5 nm) are formed in the K-PtSn@MFI sample (see **Fig. 1f**, **Fig. 1j** and **Fig. S27**).

According to the XANES results (**Fig. 2a**), Pt species also exist as metallic state in the PtSn@MFI

and K-PtSn@MFI sample. As shown in **Fig. 2b** and **Table 1**, the K-free PtSn@MFI gives a first-shell N_{Pt-Pt} of ~10.7, corresponding to Pt nanoparticles of 4-5 nm, while a first shell N_{Pt-Pt} of ~6.4 is found with the K-PtSn@MFI sample, corresponding to an average size of ~0.9 nm. These results further confirm the critical role of K^+ on stabilizing subnanometric Pt species.[18-20]

Following the same approach, we have studied the location of subnanometric Pt and Sn species in the K-PtSn@MFI sample by paired HR HAADF-STEM (see **Fig. S28** images in greyscale) and iDPC imaging. As it can be seen in **Fig. 3i-3p**, subnanometric Pt and Sn species are also located in the 10MR sinusoidal channels of MFI zeolite (see additional images in **Fig. S29** to **Fig. S33**). The oxidation state of Sn in the unreduced K-PtSn@MFI-Air sample is determined to be Sn(IV). After reduction by H_2, a decrease in the white line intensity and a redshift of the spectrum is observed in the K-PtSn@MFI sample. As shown in **Fig. 2c**, the shape of the XANES spectra of the reduced K-PtSn@MFI does not resemble either Sn metal or SnO, suggesting a possible formation of SnO_{4-x} species. This can also be supported by the reduction in the first-shell intensity of |FT| (**Fig. 2d**), indicating the loss of neighboring oxygen. The idea that Sn species are well-dispersed within the K-PtSn@MFI sample is supported by the EXAFS spectrum, since no additional higher shells are observed. Furthermore, we have found that the EXAFS spectrum of K-PtSn@MFI is different to that Sn-Beta, indicating that Sn should exist as extra-framework species (see **Fig. S35**).[29,30]

The interaction between Pt and Sn in the K-PtSn@MFI sample has been investigated by CO-IR spectroscopy. As can be seen in **Fig. S36**, the CO adsorption bands at 1887 and 1719 cm^{-1} can only be observed in the K-PtSn@MFI sample, indicating that the introduction of Sn can modulate the electronic structure of Pt clusters. These bands are probably related to the formation of bimetallic PtSn species.[31]

As shown in **Fig. 3q** to **3t**, the simulated images with Pt or Sn clusters located in the sinusoidal channels are consistent with the experimental images. According to our simulation results (**Fig. S37** and **Fig. S38**), it is possible to differentiate single Pt and Sn atoms from the zeolite framework. Indeed, we have observed a few singly dispersed atoms (Pt or Sn) in both K-Sn@MFI and K-PtSn@MFI samples (**Fig. S39** and **Fig. S40**). Considering the average particle size obtained from the EXAFS results, the amount of singly dispersed Pt atoms in the K-Pt@MFI and K-PtSn@MFI samples should be low and Pt should mainly exist as subnanometric clusters (**Fig. S41**).

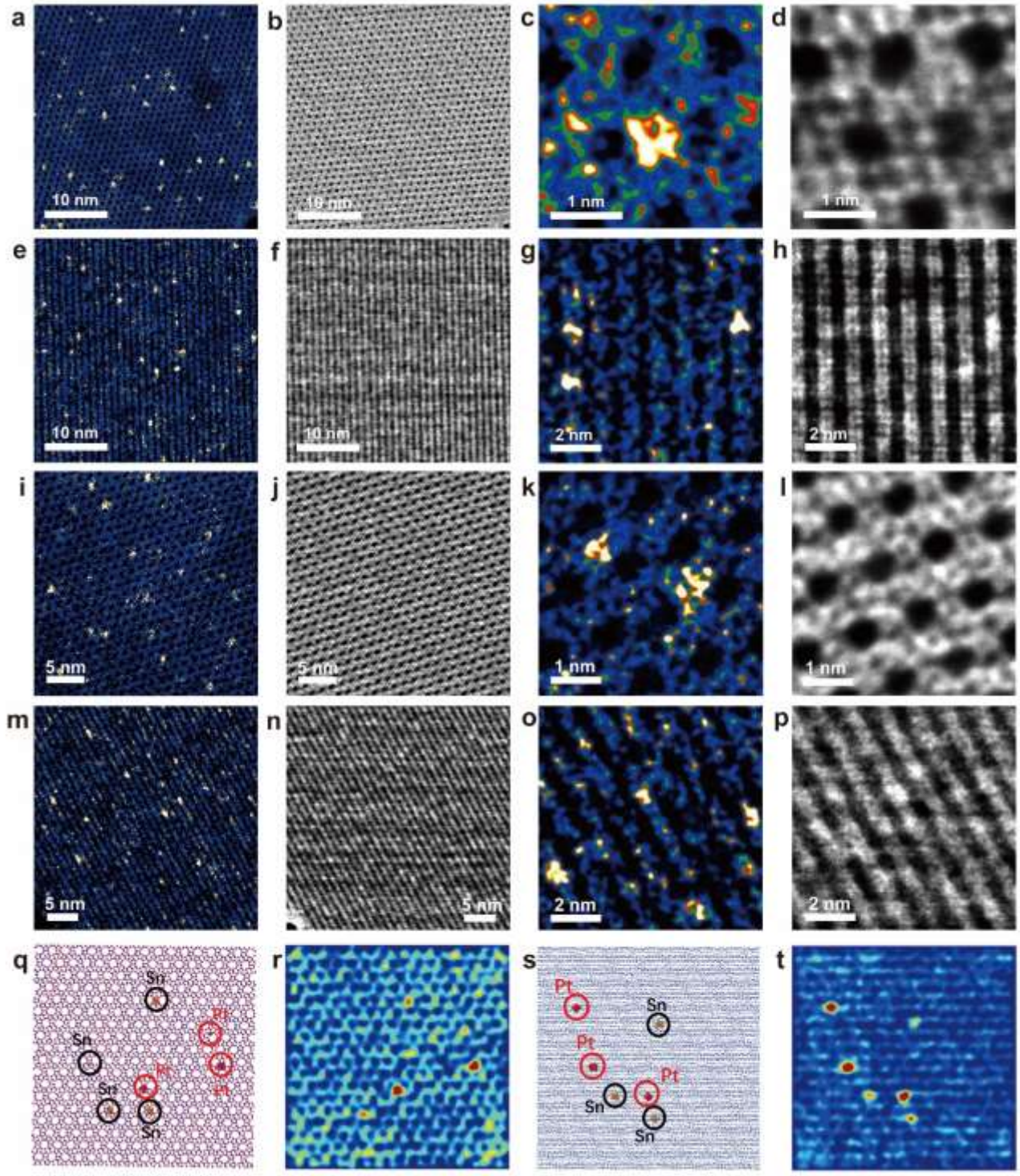

Fig. 3. Identification of the location of subnanometric Pt clusters within the MFI structure. (a, c) Large-area and detailed high-resolution HAADF-STEM image and (b, d) the corresponding iDPC image of the same area of K-Pt@MFI sample in the [010] orientation. (e, g) Large-area and detailed HAADF-STEM image and (f, h) the corresponding iDPC image of the same area of K-Pt@MFI sample in the tilted-[010] orientation. (i, k) Large-area and detailed high-resolution HAADF-STEM image and

(j, l) the corresponding iDPC image of the same area of K-PtSn@MFI sample in the [010] orientation. (m, o) Large-area and detailed HAADF-STEM image and (n, p) the corresponding iDPC image of the same area of K-PtSn@MFI sample in the tilted-[010] orientation. In the HAADF-STEM images, subnanometric Pt clusters (~0.5 nm) are clearly imaged. In the corresponding iDPC images, the atomic structures of MFI zeolite are also clearly revealed. By combing the images obtained in the two modes, we can identify the precise location of Pt species in the MFI zeolite, corresponding to the sinusoidal channels. (q) Structural model of a MFI zeolite containing a Pt single atom, a Sn single atom, Pt clusters and Sn clusters in the sinusoidal channels along the [010] orientation. (r) Simulated HAADF-STEM image of the model in (q), showing the contrasts of the different types of metal species. (s) Model of MFI zeolite containing a Pt single atom, a Sn single atom, Pt clusters and Sn clusters along the tilted-[010] orientation. (t) Simulated HAADF-STEM image of the model in (s), showing the contrasts of the different types of metal species.

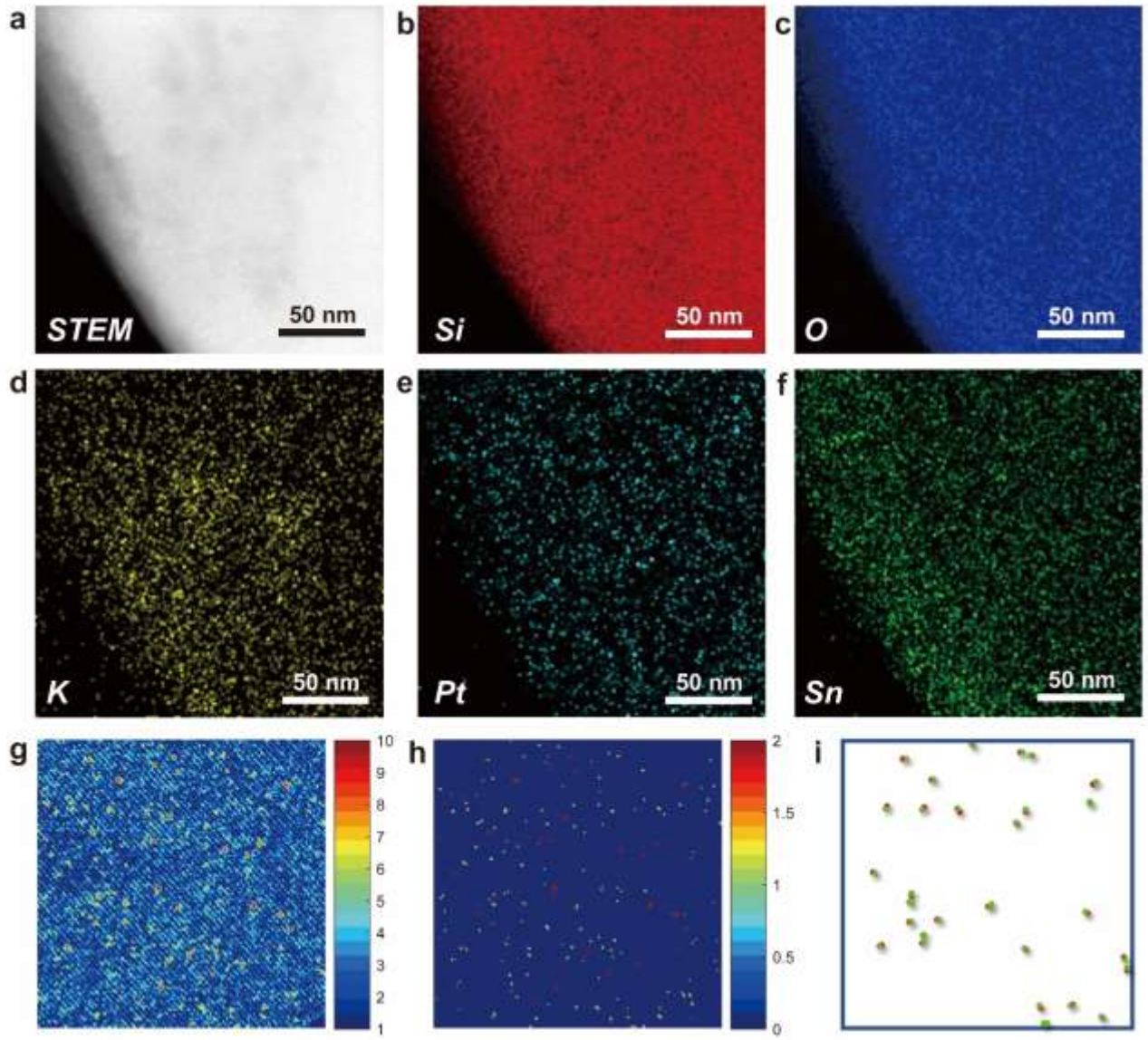

Fig. 4. Chemical analysis on the K-PtSn@MFI sample. (a-f) Elemental mapping of K-PtSn@MFI sample, showing the homogeneous distributions of K, Sn and Pt in the zeolite crystallites. (g) High-resolution HAADF-STEM image of K-PtSn@MFI sample along the tilted [010] direction. The contrasts of the subnanometric particles are displayed in pseudo color for improved visualization. (h) Automatic identification of the subnanometric Pt (red) and Sn (green) species using segmentation by K-means clustering. The contrast information in the simulation results was taken into account. (i) Location of Pt (red) and Sn (green) species with distance below 0.1 nm, which may establish interaction between them. The statistical analysis shows that, ~40% of the Pt clusters in this area are in contact with Sn species.

Determination of the Pt and Sn distribution in K-PtSn@MFI

As displayed in **Fig. 4a to 4f**, K, Sn and Pt are homogeneously distributed in the K-PtSn@MFI sample according to the X-ray energy dispersive spectroscopy (X-EDS) mapping. However, due to the resolution limitation, it is not possible to determine the relative spatial relationship between Sn and Pt. To overcome the limitation of X-EDS on such beam-sensitive samples, we have attempted, on the basis of the imaging simulation results (see **Fig. S42** to **Fig. S44**), to discriminate Pt and Sn distributions by a K-means clustering analysis of the high-resolution HAADF-STEM images (see supplementary information for details). As shown in **Fig. 4g** to **4i**, subnanometric Pt and Sn species can be identified according to their different contrast in the HR HAADF-STEM images. Then, in the image depicting the distribution of the Pt and Sn species (**Fig. 4h**) after K-means clustering, it is possible to pick out the Pt and Sn species which are in contact, simply by selecting those which fall at a distance shorter than 0.1 nm in **Fig. 4h**. This distance threshold was selected on the basis of the first-shell Sn-O distance found in the EXAFS analysis. As a result, it is possible to estimate the presence of bimetallic PtSn clusters in the K-PtSn@MFI sample made up of two neighboring Pt and Sn units rather than alloyed clusters, as shown in **Fig. 4h**. The statistical analysis shows that, ~40% of the subnanometric metal clusters automatically detected in the experimental image of **Fig. 4g** fall at a distance below 0.1 nm. It should be noted that this is a rough estimation since the image analysis is based on two-dimensional projection images. This may result in an overestimation of the fraction of bimetallic clusters, since Pt and Sn at different depths may overlap in the STEM image. The complexity of the experimental images also makes it difficult to obtain an accurate percentage of the PtSn bimetallic clusters due to the difficulty to discriminate single Pt atom and Sn cluster, as discussed in **Fig. S42** and **Fig. S43**.

Additionally, in the experimental HR HAADF-STEM images of the K-PtSn@MFI sample, we have found areas showing intensity profiles similar to those observed in simulation results (see **Fig. S45**). The formation of such subnanometric Pt-SnOx interfacial structure can explain the absence of Pt-Sn bonding in the EXAFS results, since Pt and Sn are not in the form of conventional PtSn alloy nanoparticles.[32-35]

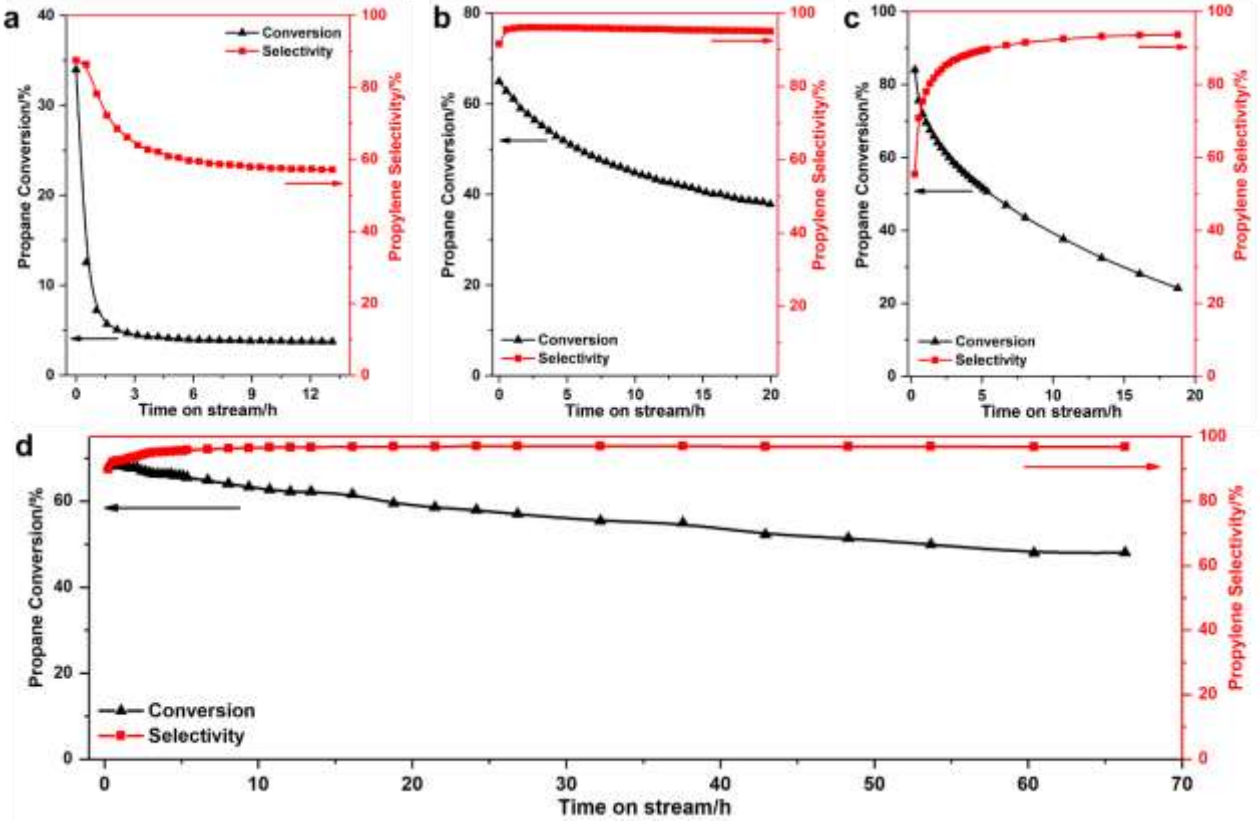

Fig. 5. Catalytic performance of Pt-zeolite materials for propane dehydrogenation reaction. First reaction cycle for propane dehydrogenation at 600 °C with (a) Pt@MFI, (b) PtSn@MFI, (c) K-Pt@MFI and (d) K-PtSn@MFI. In all the panels, the conversion of propane (black) and selectivity to propylene (red) are presented. The catalyst was reduced by H_2 at 600 °C before the atmosphere was switched to reaction feed gas. Reaction conditions: 320 mg Pt-zeolite catalyst, propane/N_2 mixture as the feed gas (5 mL/min of propane and 16 mL/min of N_2).

Catalytic studies of Pt-zeolite materials.

The dehydrogenation of propane to propylene (PDH) was chosen as model reaction to test the reactivity and stability of Pt particles or clusters encapsulated in pure-silica MFI zeolite. As can be seen in **Fig. 5a**, Pt@MFI was initially active but a fast deactivation was observed. Therefore, regeneration of the deactivated sample was carried out by a calcination treatment in air at 600 °C followed by a subsequent reduction by H_2 at 600 °C. However, fast deactivation was still observed in the second and third cycles (see **Fig. S46** and **Fig. S47**). Agglomeration of Pt nanoparticles was observed with the used Pt@MFI catalyst after three catalytic cycles (see **Fig. S48**). When Sn was

introduced as a promotor, the resultant PtSn@MFI showed a significantly enhanced activity and selectivity (see **Fig. 5b**), in consistence with previous works on supported PtSn catalysts.[36,37] However, the PtSn@MFI catalyst also suffered severe deactivation during the regeneration-reaction cycles. As displayed in **Fig. S49** and **Fig. S50**, the PtSn@MFI catalyst only showed ca. 1/3 of its initial reactivity in the third cycle, which is caused by the sintering of Pt (see **Fig. S51**). Furthermore, a high initial activity was observed with the K-Pt@MFI sample, indicating the high reactivity of subnanometric Pt clusters (see **Fig. 5c**). However, a large quantity of cracking products (methane, ethylene and ethane) were formed and the K-Pt@MFI catalyst also suffered a fast deactivation due to the coke formation. Interestingly, as demonstrated in **Fig. S52** to **Fig. S54**, the reactivity of the deactivated K-Pt@MFI catalyst can be fully recovered by calcination-reduction treatment for at least three cycles and the subnanometric Pt clusters remain stable during these processes.

According to the above results, by the combination of K and Sn, the reactivity and stability of Pt should be enhanced. Indeed, as shown in **Fig. 5d**, the K-PtSn@MFI sample shows high reactivity under the same reaction condition as used before. More importantly, the selectivity to propylene at the initial stage is already quite high (~90%) and the lifetime of the catalyst is significantly extended. It should be noted that, the K-Sn@MFI sample without Pt is not active for this reaction, indicating that Sn only modulates the reactivity of Pt. The high catalytic performance of K-PtSn@MFI can be maintained for at least three reaction-regeneration cycles without obvious deactivation (see **Fig. S55** and **Fig. S56**). The size and spatial location of the subnanometric Pt clusters are preserved after reaction, which is confirmed by EXAFS and electron spectroscopy characterizations (see **Table S4** and **Fig. S57** to **Fig. S61**). The Pt clusters in the K-PtSn@MFI sample remain to be subnanometric even after oxidation-reduction treatment at 700 °C (see **Fig. S62** and **Fig. S63**). The reactivity and recyclability of different Pt-zeolite catalysts has been compared in terms of initial turnover frequency, mass activity and deactivation rate (see **Table S5**, **Fig. S64** and **Fig. S65**). These results clearly demonstrate subnanometric PtSn clusters confined in the 10MR channels are highly stable and selective catalyst for PDH reaction.

For comparison, a reference K-PtSn/MFI sample with the same chemical composition as the K-PtSn@MFI sample was also prepared by conventional incipient wetness impregnation (see **Fig. S66**), containing well dispersed Pt particles of 0.4 to 1.2 nm. The STEM-iDPC images show that, Pt species

appear in several types of positions in MFI zeolite, including the sinusoidal channels, straight channels as well as the intersectional void (see **Fig. S67** and **Fig. S68**). As shown in **Fig. S69** and **Fig. S70**, the K-PtSn/MFI sample presented a fast deactivation during the PDH reaction and its reactivity declined after each regeneration treatment. Large Pt nanoparticles are formed in the used K-PtSn/MFI catalyst after three catalytic cycles (see **Fig. S71**), indicating the advantage of K-PtSn@MFI catalyst with regioselective location of subnanometric Pt clusters in sinusoidal channels.

3. Outlook

The concept that regioselective localization of extra-framework metal species demonstrated in this work can be extended to other crystalline porous materials, including both MOFs and zeolites. Moreover, the use of two complementary STEM-based techniques (HR HAADF-STEM and iDPC) can be a general approach for studying the position of metal species in heterogeneous metal catalysts at atomic level.

References

1. Liu, L. & Corma, A. Metal Catalysts for Heterogeneous Catalysis: From Single Atoms to Nanoclusters and Nanoparticles. *Chem. Rev.* **118**, 4981-5079 (2018).
2. Gallego, E. M. *et al.* "Ab initio" synthesis of zeolites for preestablished catalytic reactions. *Science* **355**, 1051-1054 (2017).
3. Kosinov, N., Liu, C., Hensen, E. J. M. & Pidko, E. A. Engineering of Transition Metal Catalysts Confined in Zeolites. *Chem. Mater.* **30**, 3177-3198 (2018).
4. Ortalan, V., Uzun, A., Gates, B. C. & Browning, N. D. Direct imaging of single metal atoms and clusters in the pores of dealuminated HY zeolite. *Nat. Nanotechnol.* **5**, 506-510 (2010).
5. Li, C. *et al.* Selective Introduction of Acid Sites in Different Confined Positions in ZSM-5 and Its Catalytic Implications. *ACS Catal.* **8**, 7688-7697 (2018).
6. Knott, B. C. *et al.* Consideration of the Aluminum Distribution in Zeolites in Theoretical and Experimental Catalysis Research. *ACS Catal.* **8**, 770-784 (2017).
7. Yokoi, T., Mochizuki, H., Namba, S., Kondo, J. N. & Tatsumi, T. Control of the Al Distribution in the Framework of ZSM-5 Zeolite and Its Evaluation by Solid-State NMR Technique and Catalytic Properties. *J. Phys. Chem. C* **119**, 15303-15315 (2015).
8. Goel, S., Zones, S. I. & Iglesia, E. Encapsulation of metal clusters within MFI via interzeolite transformations and direct hydrothermal syntheses and catalytic consequences of their confinement. *J. Am. Chem. Soc.* **136**, 15280-15290 (2014).
9. Wang, N. *et al.* In Situ Confinement of Ultrasmall Pd Clusters within Nanosized Silicalite-1 Zeolite for Highly Efficient Catalysis of Hydrogen Generation. *J. Am. Chem. Soc.* **138**, 7484-7487 (2016).
10. Iida, T., Zanchet, D., Ohara, K., Wakihara, T. & Roman-Leshkov, Y. Concerted Bimetallic Nanocluster Synthesis and Encapsulation via Induced Zeolite Framework Demetallation for Shape and Substrate Selective Heterogeneous Catalysis. *Angew. Chem. Int. Ed.* **57**, 6454-6458 (2018).
11. Zhang, J. *et al.* Sinter-resistant metal nanoparticle catalysts achieved by immobilization within zeolite crystals via seed-directed growth. *Nat. Catal.* **1**, 540-546 (2018).
12. Campbell, C. T., Parker, S. C. & Starr, D. E. The effect of size-dependent nanoparticle energetics on catalyst sintering. *Science* **298**, 811-814 (2002).
13. Flytzani-Stephanopoulos, M. & Gates, B. C. Atomically dispersed supported metal catalysts. *Ann. Rev. Chem. Biomol. Eng.* **3**, 545-574 (2012).
14. Liu, L. *et al.* Generation of subnanometric platinum with high stability during transformation of a 2D zeolite into 3D. *Nat. Mater.* **16**, 132-138 (2017).
15. Liu, L. *et al.* Evolution and stabilization of subnanometric metal species in confined space by in situ TEM. *Nat. Commun.* **9**, 574 (2018).
16. Xiong, H. *et al.* Thermally Stable and Regenerable Platinum-Tin Clusters for Propane Dehydrogenation Prepared by Atom Trapping on Ceria. *Angew. Chem. Int. Ed.* **56**, 8986-8991 (2017).
17. Sattler, J. J., Ruiz-Martinez, J., Santillan-Jimenez, E. & Weckhuysen, B. M. Catalytic dehydrogenation of light alkanes on metals and metal oxides. *Chem. Rev.* **114**, 10613-10653 (2014).
18. Zhu, J. *et al.* Size-Dependent Reaction Mechanism and Kinetics for Propane Dehydrogenation over Pt Catalysts. *ACS Catal.* **5**, 6310-6319 (2015).
19. Yang, M. *et al.* A common single-site Pt(II)-O(OH)x- species stabilized by sodium on "active" and "inert" supports catalyzes the water-gas shift reaction. *J. Am. Chem. Soc.* **137**, 3470-3473 (2015).

20. Yang, M. *et al.* Catalytically active Au-O(OH)x-species stabilized by alkali ions on zeolites and mesoporous oxides. *Science* **346**, 1498-1501 (2014).
21. Zhai, Y. *et al.* Alkali-stabilized Pt-OHx species catalyze low-temperature water-gas shift reactions. *Science* **329**, 1633-1636 (2010).
22. Lazic, I., Bosch, E. G. T. & Lazar, S. Phase contrast STEM for thin samples: Integrated differential phase contrast. *Ultramicroscopy* **160**, 265-280 (2016).
23. Yucelen, E., Lazic, I. & Bosch, E. G. T. Phase contrast scanning transmission electron microscopy imaging of light and heavy atoms at the limit of contrast and resolution. *Sci. Rep.* **8**, 2676 (2018)
24. Van Koningsveld, H. On the location and disorder of the tetrapropylammonium (TPA) ion in zeolite ZSM-5 with improved framework accuracy. *Acta Cryst.* B **43**, 127-132 (1987).
25. Dib, E., Grand, J., Mintova, S. & Fernandez, C. Structure-Directing Agent Governs the Location of Silanol Defects in Zeolites. *Chem. Mater.* **27**, 7577-7579, (2015).
26. Denayer, J. F., De Meyer, K., Martens, J. A. & Baron, G. V. Molecular competition effects in liquid-phase adsorption of long-chain n-alkane mixtures in ZSM-5 zeolite pores. *Angew. Chem. Int. Ed.* **42**, 2774-2777 (2003).
27. Grand, J. *et al.* One-pot synthesis of silanol-free nanosized MFI zeolite. *Nat. Mater.* **16**, 1010-1015 (2017).
28. de Graaf, J., van Dillen, A. J., de Jong, K. P. & Koningsberger, D. C. Preparation of Highly Dispersed Pt Particles in Zeolite Y with a Narrow Particle Size Distribution: Characterization by Hydrogen Chemisorption, TEM, EXAFS Spectroscopy, and Particle Modeling. *J. Catal.* **203**, 307-321 (2001).
29. Bare, S. R. *et al.* Uniform catalytic site in Sn-beta-zeolite determined using X-ray absorption fine structure. *J. Am. Chem. Soc.* **127**, 12924-12932 (2005).
30. Hammond, C. *et al.* Identification of Active and Spectator Sn Sites in Sn-beta Following Solid-State Stannation, and Consequences for Lewis Acid Catalysis. *ChemCatChem* **7**, 3322-3331 (2015).
31. Stakheev, A. Y., Shpiro, E. S., Jaeger, N. I. & Schulz-Ekloff, G. Electronic state and location of Pt metal clusters in KL zeolite: FTIR study of CO chemisorption. *Catal. Lett.* **32**, 147-158 (1995).
32. Huang, H. *et al.* Effects of heat treatment atmosphere on the structure and activity of Pt_3Sn nanoparticle electrocatalysts: a characterization case study. *Faraday Discussions* **208**, 555-573 (2018).
33. Alexeev, O. S. & Gates, B. C. Supported Bimetallic Cluster Catalysts. *Ind. Eng. Chem. Res.* **42**, 1571-1587 (2003).
34. Sankar, M. *et al.* Designing bimetallic catalysts for a green and sustainable future. *Chem. Soc. Rev.* **41**, 8099-8139 (2012).
35. Ferrando, R., Jellinek, J. & Johnston, R. L. Nanoalloys: from theory to applications of alloy clusters and nanoparticles. *Chem. Rev.* **108**, 845-910 (2008).
36. Zhu, H. *et al.* Sn surface-enriched Pt–Sn bimetallic nanoparticles as a selective and stable catalyst for propane dehydrogenation. *J. Catal.* **320**, 52-62 (2014).
37. Wu, J., Peng, Z. & Bell, A. T. Effects of composition and metal particle size on ethane dehydrogenation over Pt_xSn_{100-x}/Mg(Al)O ($70 \leqslant x \leqslant 100$). *J. Catal.* **311**, 161-168 (2014).

Acknowledgements

This work has been supported by the European Union through the European Research Council (grant ERC-AdG-2014-671093, SynCatMatch) and the Spanish government through the "Severo Ochoa Program" (SEV-2016-0683). L.L. thanks ITQ for providing a contract. The authors also thank Microscopy Service of UPV for the TEM and STEM measurements. The XAS measurements were carried out in CLAESS beamtime of ALBA synchrotron. High-resolution STEM measurements were performed at DME-UCA in Cadiz University with financial support from FEDER/MINECO (MAT2017-87579-R and MAT2016-81118-P). A relevant patent application (European patent application No. 19382024.8) has been presented.

Author Contribution

A.C. conceived the project, directed the study and wrote the manuscript. L.L. carried out the synthesis, characterizations, catalytic measurements and collaborated in writing the manuscript. M.L.-H. and J.J.C. carried out the high-resolution STEM measurements, image analysis and simulations. C.W.L. carried out the analysis of XAS data. L.L., C.L. and L.S. contributed to the collection of XAS data in ALBA synchrotron. P.C. carried out the CO-IR adsorption experiments. All the authors discussed the results and contributed to the formation of the manuscript.

Additional information

Supplementary information is available in the online version of the paper. Reprints and permissions information is available online at www.nature.com/reprints. Correspondence and requests for materials should be addressed to A.C.

Methods

One-pot synthesis of MFI zeolites with the encapsulation of Pt

Synthesis of Pt@MFI material (Pt nanoparticles encapsulated in purely siliceous MFI)

Pt nanoparticles encapsulated in MFI zeolite were prepared by a one-pot synthesis. Firstly, a tetrapropylammonium hydroxide (TPAOH) solution was prepared by mixing 8.12 g of K-free TPAOH solution (40 wt%, from Alfa-Aesar, product code: 17456.22) and 20.1 g of distilled water at room temperature. Then, 8.24 g Tetraethyl orthosilicate (TEOS) was hydrolyzed with the TPAOH solution at room temperature for 6 h under stirring (500 rpm). The resultant solution was divided into two parts with the same weight. To each portion of the solution, 80 μL H_2PtCl_6 aqueous (0.38 mol/L) and 150 μL of ethylenediamine were added while stirring was kept for 10 min. The resultant yellow solution was then transferred to Teflon-lined autoclaves and heated in an electric oven at 175 ºC for 96 h under static conditions. The amount of Pt in the final product is 0.43 wt%. After the hydrothermal process, the solid product was isolated by filtration and washed with distilled water and acetone and then dried at 60 ºC. Then the solid sample was calcined under an air flow at 560 ºC for 8 h and then at 600 ºC for 2 h.

Synthesis of PtSn@MFI material (PtSn nanoparticles encapsulated in purely siliceous MFI)

Bimetallic PtSn nanoparticles encapsulated in MFI zeolite were prepared by a one-pot synthesis. Firstly, a tetrapropylammonium hydroxide (TPAOH) solution was prepared by mixing 8.12 g of K-free TPAOH (40 wt%, from Alfa-Aesar, product code: 17456.22) and 20.1 g of distilled water at room temperature. Then, 8.24 g Tetraethyl orthosilicate (TEOS) was hydrolyzed with tetrapropylammonium hydroxide solution (TPAOH) at room temperature for 6 h under stirring (500 rpm). The resultant solution was divided into two parts with the same weight. To each portion of the solution, 80 μL of H_2PtCl_6 aqueous (0.38 mol/L), 28 mg of $SnCl_4$ and 150 μL of ethylenediamine were added while stirring was kept for 10 min. The resultant yellow solution was then transferred to Teflon-lined autoclaves and heated in an electric oven at 175 ºC for 96 h under static conditions. The amounts of Pt and Sn in the final product were 0.44 wt % and 1.0 wt%, respectively. After the hydrothermal process, the solid product was isolated by filtration and washed with distilled water and acetone and then dried

at 60 ºC. Then the solid sample was calcined under air flow at 560 ºC for 8 h and then at 600 ºC for 2 h.

Synthesis of K-Pt@MFI (K-promoted Pt clusters encapsulated in purely siliceous MFI)

K-promoted Pt clusters encapsulated in MFI zeolite were prepared by a one-pot synthesis. Firstly, a tetrapropylammonium hydroxide (TPAOH) solution was prepared by mixing 5.0 g of K-free TPAOH solution (40 wt%, from Alfa-Aesar, product code: 17456.22) and 6.24 g of TPAOH solution (20 wt%, from Sigma-Aldrich, containing ~0.6 wt% of K, product code: 254533-100G) and 17.0 g of distilled water at room temperature. Then, 8.24 g Tetraethyl orthosilicate (TEOS) were hydrolyzed with the TPAOH solution at room temperature for 6 h under stirring (500 rpm). The resultant solution was divided into two parts with the same weight. To each portion of the solution, 80 μL of H_2PtCl_6 aqueous (0.38 mol/L) and 150 μL of ethylenediamine were added and stirring was kept for 10 min. The resultant yellow solution was then transferred to Teflon-lined autoclaves and heated in an electric oven at 175 ºC for 96 h under static conditions. The amounts of Pt and K in the final product were 0.42 wt% and 0.6 wt%, respectively. After the hydrothermal process, the solid product was isolated by filtration and washed with distilled water and acetone and then dried at 60 ºC. Then the solid sample was calcined under air flow at 560 ºC for 8 h and then at 600 ºC for 2 h.

Synthesis of K-PtSn@MFI (K-promoted PtSn bimetallic clusters encapsulated in purely siliceous MFI)

K-promoted PtSn bimetallic clusters encapsulated in MFI zeolite were prepared by a one-pot synthesis. Firstly, a tetrapropylammonium hydroxide (TPAOH) solution was prepared by mixing 5.0 g K-free TPAOH solution (40 wt%, from Alfa-Aesar without K, product code: 17456.22) and 6.24 g TPAOH (20 wt% from Sigma-Aldrich, containing ~0.6 wt% of K, product code: 254533-100G) and 17.0 g of distilled water at room temperature. Then, 8.24 g Tetraethyl orthosilicate (TEOS) were hydrolyzed with the TPAOH solution at room temperature for 6 h under stirring (500 rpm). The resultant solution was divided into two parts with the same weight. To each portion of the solution, 80 μL of H_2PtCl_6 aqueous (0.38 mol/L), 50 mg of $SnCl_4 \cdot 5H_2O$ and 150 μL of ethylenediamine were added to the above solution and the mixture kept under stirring for 10 min. The resultant yellow solution was then

transferred to Teflon-lined autoclaves and heated in an electric oven at 175 ºC for 96 h under static conditions. The amounts of Pt, Sn and K in the final product were 0.42 wt%, 0.9 wt% and 0.65 wt%, respectively. After the hydrothermal process, the solid product was isolated by filtration and washed with distilled water and acetone and then dried at 60 ºC. Then the solid sample was calcined under air flow at 560 ºC for 8 h and then at 600 ºC for 2 h.

Synthesis of K-PtSn/MFI by conventional incipient wetness impregnation.

Firstly, a K-promoted purely siliceous MFI support was prepared. 5.0 g K-free TPAOH solution (40 wt%, from Alfa-Aesar without K, product code: 17456.22) and 6.24 g TPAOH (20 wt% from Sigma-Aldrich containing ~0.6 wt% of K, product code: 254533-100G) and 17.0 g of distilled water at room temperature. Then, 8.24 g Tetraethyl orthosilicate (TEOS) were hydrolyzed with the TPAOH solution at room temperature for 6 h under stirring (500 rpm). The resultant solution was divided into two parts with the same weight and then transferred to Teflon-lined autoclaves and heated in an electric oven at 175 ºC for 96 h under static conditions. After the hydrothermal process, the solid product was isolated by filtration and washed with distilled water and acetone and then dried at 60 ºC. Then the solid sample was calcined under air flow at 560 ºC for 8 h and then at 600 ºC for 2 h.

Taking that K-MFI as support, Pt and Sn together with ethylenediamine is introduced to the K-MFI support by conventional incipient wetness impregnation. The amount of Pt and Sn is the same to the K-PtSn@MFI sample prepared by one-pot synthesis.

Characterization

Powder X-ray diffraction (XRD) was performed with a HTPhilips X'Pert MPD diffractometer equipped with a PW3050 goniometer using Cu Kα radiation and a multisampling handler.

Samples for electron microscopy studies were prepared by dropping the suspension of the solid samples in CH_2Cl_2 directly onto holey-carbon coated copper grids. Electron Microscopy measurements were performed using two types of microscopes. Thus, non-corrected JEOL 2100F microscope operating at 200 kV both in transmission (TEM) and scanning-transmission modes (STEM) was used to record High Angle Annular Dark-Field (HAADF), Z-contrast, images at low resolution. High-resolution HAADF-STEM and STEM-iDPC imaging was performed on a double aberration

corrected (AC), monochromated, FEI Titan^3 Themis 60-300 microscope working at 300 kV. The last technique, iDPC (integrated-Differential Phase Contrast) imaging, provides in this microscope atomically resolved images in which the contrasts are related to the atomic number of the elements under the beam, instead of the roughly Z^2-dependent contrasts obtained in HAADF-STEM images. By using a 4-segment detector, this technique allows imaging light elements, as it is the case of O, in the presence of heavier ones (Si, Z=14) under very low electron dose conditions, which is a key aspect in the atomic scale structural analysis of zeolites, which are very sensitive to electron beams. In particular, 2048×2048 HAADF-iDPC image pairs were recorded simultaneously using a convergence angle of 18.6 mrad and a camera length of 91 mm. This configuration allowed us to optimize the collection of the signals on the HAADF and FEI DF4 detectors. In order to limit the damage by the electron beam, a fast image recording protocol was used by combining a beam current of 30 pA, a 2.5 μs dwell time and an automated fine-tuning alignment of A1 and C1 using the OptiSTEM software. To obtain images with good quality, the beam current and image acquisition time should be optimized according to the stability of the sample under the beam.

The microscope was also used to perform chemical mapping at medium magnifications (approximately 100 K to 200 K) by STEM X-Ray Energy Dispersive Spectroscopy (XEDS) using the high-efficiency SuperX G2 detection system equipped in the microscope, which integrates 4 windowless detectors surrounding the sample and a high-performance signal processing hardware. STEM-XEDS was used to map the spatial distribution of both metallic (Sn, Pt, K) and non-metallic elements (Si, O). For this nanoanalytical experiments, the beam current was increased up to 100 pA and the dwell time to 128 μs in order to obtain a good signal-to-noise ratio. Then, the elemental maps were background subtracted and smoothed by 3×3 pixels averaging.

To determine the spatial distribution of the metallic species within the zeolite framework, a specific methodology for the digital analysis of the experimental images has been developed and coded in a home-made Matlab script. First, to improve the signal-to-noise, the HR HAADF STEM images were denoised by combining the Anscomb transform and Undecimated Wavelet Transforms (UWVT).[38] Then, a user-independent, fully automated, segmentation of image contrasts by clustering techniques (K-means method) was applied to recognize and classify the metallic entities, which is a requirement to guarantee statistically meaningful and unbiased results.

To support the K-means clustering analysis and interpreting the details of the experimental images HR HAADF-STEM image simulation was carried out using TEMSIM software.[39] The complex structural models used as input in these simulations were built using the Rhodius software developed at UCA.[40] To approach as close as possible to the experimental imaging conditions, a mixture of Poisson and white Gaussian noise was added to the simulated images. Then, the same methodology used to analyze the experimental images was applied to the on-purpose noise-corrupted simulated images.

X-ray absorption experiments at the Pt (11564 eV) L_{III} and Sn (29200 eV) K-edges, were performed in ALBA synchrotron.[41] The beam was monochromatized using a Si (111) and (311) double crystals, respectively; harmonic rejection has been performed using Rh-coated silicon mirrors. The spectra were collected in transmission (Pt L_{III}-edge) and fluorescence (Sn K-edge) modes by means of the ionization chambers filled with appropriate gases (Pt L_{III}-edge: 95 % N_2 + 5 % Kr for I_0 and 17.1 % N_2 + 82.9 % Kr for I_1; Sn K-edge: 89.4 % N_2 + 10.6 % Kr for I_0 and 100 % Kr for I_1) and a fluorescence solid-state detector. Samples in the form of self-supported pellets of optimized thickness have been located inside an in-house built multipurpose cell described by Guilera allowing *in situ* experiments.[42] Several scans were acquired at each measurement step to ensure spectral reproducibility and good signal-to-noise ratio. The data reduction and extraction of the $\chi(k)$ function has been performed using Athena code.[43] EXAFS data analysis has been performed using the Arthemis software.[43] Phase and amplitudes have been calculated by FEFF6 code. The values of E_0 (inflection point in the first derivative of XANES spectra) used for data alignment taken from literature were the following: 29200 eV for Sn metal, 29201 eV for SnO, 29204 eV for SnO_2 and 11564 eV for Pt metal.

IR spectra of adsorbed CO on Pt-zeolite and Sn-zeolite samples were recorded at room temperature with a Nexus 8700 FTIR spectrometer using a DTGS detector and acquiring at 4 cm^{-1} resolution. An IR cell allowing in situ treatments in controlled atmospheres and temperatures from 25 °C to 500 °C has been connected to a vacuum system with gas dosing facility. For IR studies the samples were pressed into self-supported wafers and pre-treated in H_2 flow at 450 °C for 2 h followed by vacuum treatment (10^{-5} mbar). After activation the samples were cooled down to 25 °C under dynamic vacuum conditions followed by CO dosing at increasing pressure (0.4-8.5 mbar). IR spectra were recorded after each dosage of CO.

The dispersion of Pt in Pt-zeolite materials was estimated from CO adsorption using the double isotherm method on a Quantachrome Autosorb-1C equipment.[44,45] Prior to adsorption, the samples (200-300 mg) were reduced in situ in flowing pure H_2 (25 mL/min) at 600 ºC for 1 h with a ramp rate of 5 ºC/min from room temperature to 600 ºC. After the reduction treatment, the samples were degassed at 1.33 Pa for 2 h at 600 ºC and then cool to ~40 ºC. Then pure CO was admitted and the first adsorption isotherm (i.e. the total CO uptake) was measured. After evacuation at 25 ºC, the second isotherm (i.e. the reversible CO uptake) was measured. The amount of chemisorbed CO was then obtained by subtracting the two isotherms. The pressure range studied was 0.5-11 $\times 10^4$ Pa. The dispersion of Pt (D) was calculated from the amount of irreversibly adsorbed CO assuming a stoichiometry of Pt/CO=1. The mean particle size (d) of Pt was determined from chemisorption data assuming spherical geometry for the metal particle according to the procedure. Equations used for calculation of metal dispersion and metal particle size are shown below.

$D\ (\%)=N_m \times F_s \times M \times 10^4 / L$

N_m: chemisorption uptake expressed in mol of CO per gram of sample;

F_s: adsorption stoichiometry, which is 1 in our measurement;

M: molecular weight of the supported metal (Pt)

L: loading of the supported metal.

$d=6 \times L/(S_a \times Z \times 100)$

d: mean particle size

Z: density of the supported metal (Pt)

S_a: active surface area (m^2/g_{metal}) calculated from the following equation: $S_a=N_m \times F_s \times A_m \times N_a$

A_m: cross-sectional area occupied by each active surface Pt atom

N_a: Avogadro's constant

Catalytic studies of Pt-zeolite materials for propane dehydrogenation reactions.

The dehydrogenation of propane to propylene was chosen as model reaction to test the reactivity and stability of Pt particles or clusters encapsulated in pure-silica MFI zeolite. The reaction was performed with a fix-bed reactor under atmospheric pressure using N_2/propane as feed gas at 600 ºC. The products were analyzed by a GC which can detect cracking products (methane, ethene and ethane), propylene, C4, C5 and aromatics. Before reaction, the catalyst was reduced by H_2 flow (35 mL/min) at 600 ºC for

1 h with a ramp rate of 10 ºC/min from room temperature up to 600 ºC. After the reduction pre-treatment, the atmosphere was changed to reaction feed gas (5 mL/min of propane and 16 mL/min of N_2 as balanced gas). After the propane dehydrogenation test, the sample was cooled down to ~100 ºC and started to be regenerated by calcination in air at 600 ºC for 2 h with a ramp rate of 10 ºC/min from ~100 ºC up to 600 ºC. After calcination in air, the sample was cooled down to ~100 ºC again and then reduced by H_2 at 600 ºC for 1 h ~100 ºC up to 600 ºC before the second cycle for propane dehydrogenation reaction. After the second cycle of propane dehydrogenation test, the sample was cooled down to ~100 ºC and started to be regenerated by calcination in air at 600 ºC for 2 h with a ramp rate of 10 ºC/min from ~100 ºC up to 600 ºC. After calcination in air, the sample was cooled down to ~100 ºC again and then reduced by H_2 at 600 ºC for 1 h ~100 ºC up to 600 ºC before the third cycle for propane dehydrogenation reaction.

Data availability

All the data reported in this paper are available from the corresponding author upon request.

References for Methods:

38. M. López-Haro, M. Tinoco, S. Fernández-Garcia, X. Chen, A. B. Hungria, M. Á. Cauqui, J. J. Calvino, A Macroscopically Relevant 3D-Metrology Approach for Nanocatalysis Research. *Particle Particle Systems Characterization* **35**, 1700343 (2018).
39. E. J. Kirkland, *Advanced Computing in Electron Microscopy*. Springer, **2010**.
40. S. Bernal, F. J. Botana, J. J. Calvino, C. López-Cartes, J. A. Pérez-Omil, J. M. Rodríguez-Izquierdo, The interpretation of HREM images of supported metal catalysts using image simulation: profile view images. *Ultramicroscopy* **72**, 135-164 (1998).
41. L. Simonelli, C. Marini, W. Olszewski, M. Avila Perez, N. Ramanan, G. Guilera, V. Cuartero, K. Klementiev, N. L. Saini, CLÆSS: The hard X-ray absorption beamline of the ALBA CELLS synchrotron. *Cogent Physics* **3**, (2016).
42. G. Guilera, F. Rey, J. Hernández-Fenollosa, J. J. Cortés-Vergaz, One body, many heads; the Cerberus of catalysis. A new multipurpose in-situ cell for XAS at ALBA. *J. Phys. Conference Series* **430**, 012057 (2013).
43. B. Ravel, M. Newville, ATHENA, ARTEMIS, HEPHAESTUS: data analysis for X-ray absorption spectroscopy using IFEFFIT. *J. Synchrotron Rad.* **12**, 537-541 (2005).
44. Yin, F., Ji, S., Wu, P., Zhao, F. & Li, C. Deactivation behavior of Pd-based SBA-15 mesoporous silica catalysts for the catalytic combustion of methane. *J. Catal.* **257**, 108-116 (2008).
45. Allian, A. D. *et al.* Chemisorption of CO and mechanism of CO oxidation on supported platinum nanoclusters. *J. Am. Chem. Soc.* **133**, 4498-4517 (2011).